

Linearly polarized X-ray fluorescence computed tomography based on a Thomson scattering light source: a Monte Carlo study

Zhijun Chi,^{a*} Yingchao Du,^{b*} Wenhui Huang^b and Chuanxiang Tang^b

Received 18 August 2019

Accepted 9 March 2020

Edited by A. Stevenson, Australian Synchrotron, Australia

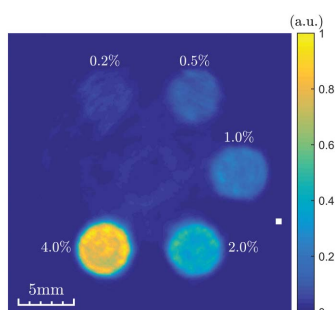
Keywords: fluorescence computed tomography; Thomson scattering X-ray source; linear polarization; scattering suppression; Monte Carlo.

^aKey Laboratory of Beam Technology of Ministry of Education, College of Nuclear Science and Technology, Beijing Normal University, Beijing 100875, People's Republic of China, and ^bKey Laboratory of Particle and Radiation Imaging of Ministry of Education, Department of Engineering Physics, Tsinghua University, Beijing 100084, People's Republic of China. *Correspondence e-mail: chizj18@bnu.edu.cn, dych@mail.tsinghua.edu.cn

A Thomson scattering X-ray source can provide quasi-monochromatic, continuously energy-tunable, polarization-controllable and high-brightness X-rays, which makes it an excellent tool for X-ray fluorescence computed tomography (XFCT). In this paper, we examined the suppression of Compton scattering background in XFCT using the linearly polarized X-rays and the implementation feasibility of linearly polarized XFCT based on this type of light source, concerning the influence of phantom attenuation and the sampling strategy, its advantage over *K*-edge subtraction computed tomography (CT), the imaging time, and the potential pulse pile-up effect by Monte Carlo simulations. A fan beam and pinhole collimator geometry were adopted in the simulation and the phantom was a polymethyl methacrylate cylinder inside which were gadolinium (Gd)-loaded water solutions with Gd concentrations ranging from 0.2 to 4.0 wt%. Compared with the case of vertical polarization, Compton scattering was suppressed by about 1.6 times using horizontal polarization. An accurate image of the Gd-containing phantom was successfully reconstructed with both spatial and quantitative identification, and good linearity between the reconstructed value and the Gd concentration was verified. When the attenuation effect cannot be neglected, one full cycle (360°) sampling and the attenuation correction became necessary. Compared with the results of *K*-edge subtraction CT, the contrast-to-noise ratio values of XFCT were improved by 2.03 and 1.04 times at low Gd concentrations of 0.2 and 0.5 wt%, respectively. When the flux of a Thomson scattering light source reaches 10^{13} photons s^{-1} , it is possible to finish the data acquisition of XFCT at the minute or second level without introducing pulse pile-up effects.

1. Introduction

Recently, Thomson scattering (also called inverse Compton scattering) X-ray sources have drawn much attention in the X-ray imaging field due to their excellent beam qualities. Based on the collision of intense laser and relativistic electrons, a Thomson scattering X-ray source can generate quasi-monochromatic, continuously energy-tunable, polarization-controllable and high-brightness X-rays, filling the performance gap between large-scale synchrotron radiation facilities and conventional X-ray tubes. It provides a valuable prospect for X-ray fluorescence computed tomography (XFCT) – a new imaging modality combining the high sensitivity of X-ray fluorescence analysis (XRF) and the high resolution of computed tomography (CT). The typical X-ray energy region (10–100 keV) of this type of light source can cover almost all biomedical applications of XFCT, and its quasi-monochromaticity will help to improve the sensitivity of XFCT. Furthermore, the small footprint, moderate cost and large



field of view (FOV) makes it very suitable for laboratory- and hospital-scale imaging application.

In this paper, we will investigate the feasibility of XFCT based on this type of light source by Monte Carlo simulations. The suppression of Compton scattering background using X-rays with linear polarization will be demonstrated. The influence of attenuation effect, sampling interval and incident X-ray photon number on image reconstruction will be discussed. Besides, the advantage of XFCT over *K*-edge subtraction CT will also be examined. Finally, the imaging time and potential pulse pile-up effect of XFCT using this type of light source will be estimated.

2. Principles and methods

2.1. Theoretical basis of scattering suppression

In the Thomson scattering of relativistic electrons with an infrared laser, the polarization characteristics of laser photons can be easily transferred to X-rays (Petrillo *et al.*, 2015). Hence, linearly polarized X-rays can be generated straightforwardly in a Thomson scattering light source by adjusting the polarization of the laser beam. For X-rays with linear polarization, their differential cross section of Compton scattering is described by the Klein–Nishina formula,

$$\frac{d\sigma_{\text{KN,LP}}}{d\Omega} = \frac{1}{2} r_e^2 e^2 (\varepsilon + \varepsilon^{-1} - 2 \sin^2 \theta \cos^2 \phi), \quad (1)$$

where $r_e = 2.82 \times 10^{-15}$ m is the classical electron radius, θ and ϕ are the polar angle and azimuthal angle, respectively, and ε is the energy ratio between the Compton scattered photon E_f and the incident photon E_i ,

$$\varepsilon = \frac{E_f}{E_i} = \frac{1}{1 + (E_i/m_e c^2)(1 - \cos \theta)}, \quad (2)$$

where $m_e c^2 = 0.511$ MeV is the rest energy of electron. At the direction of $\theta = 90^\circ/270^\circ$ and $\phi = 0^\circ/180^\circ$, the differential cross section reaches its minimum value, as shown in Fig. 1. Hence, the single Compton scattering background in XFCT will be greatly reduced when an X-ray fluorescence detector is placed in this direction, which is the theoretical basis of scattering suppression based on linearly polarized X-rays.

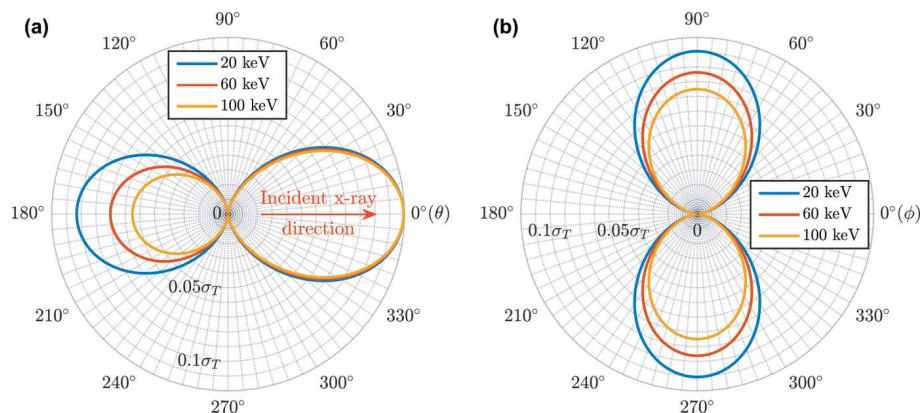


Figure 1 Differential Compton scattering cross sections at different X-ray energies in angular coordinate: (a) $\phi = 0^\circ/180^\circ$, (b) $\theta = 90^\circ/270^\circ$. $\sigma_T = 6.65 \times 10^{-25}$ cm² is the total Thomson scattering cross section.

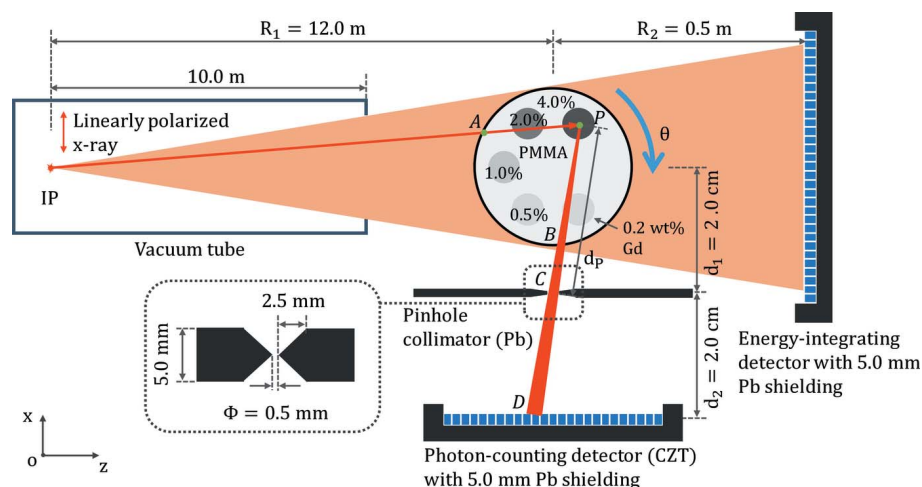


Figure 2 Schematic for XFCT based on a Thomson scattering X-ray source (not to scale).

2.2. Monte Carlo simulation

To demonstrate the feasibility of XFCT based on a Thomson scattering X-ray source, a Monte Carlo simulation was performed using the *Geant4* toolkit (Agostinelli *et al.*, 2003) (version 10.05). A fan beam imaging geometry was adopted in our simulation as the FOV of a Thomson scattering light source is very large, usually on the centimetre scale. The layout of the XFCT simulation is shown in Fig. 2. X-rays were generated at the interaction point (IP) (Chi *et al.*, 2018a) of the electron bunch and the laser beam, and then propagated 12.0 m in the *z*-axis direction before reaching the sample. The X-rays were linearly polarized in the *x*-axis (horizontal) direction and can be tuned in the *y*-axis (vertical) direction when a polarization-based comparison simulation is carried out. The source spot size used in this simulation was 10.0 μ m root mean square (r.m.s.) and the X-ray energy was 60 keV with an r.m.s. bandwidth of 1.0%. All the source parameters in the simulation, such as the source spot size (Chi *et al.*, 2018a) and bandwidth (Hartemann *et al.*, 2005), can be easily achieved based on the existing technology. The reason why we choose such a long source-to-sample distance (12.0 m) is to

limit the bandwidth of scattered X-rays caused by the energy-angle effect (Chi *et al.*, 2017a) of a Thomson scattering light source. A photon-counting detector, made of cadmium zinc telluride (CZT), was placed perpendicular to the x -axis in the x - z plane for the lowest scattering background according to the scattering suppression theory in Section 2.1. The detector was modelled using parameters that are available at present (Taguchi & Iwanczyk, 2013) – a pixel size of 100 μm and energy range of 20–100 keV. For simplicity, other parameters were assumed to be ideal, *e.g.* ideal energy resolution, 100% detection efficiency, no dark current, no readout noise and no Poisson statistics. The distance between the photon-counting detector and the sample was 4.0 cm. In the middle of them was a pinhole collimator of diameter 0.5 mm and thickness 5.0 mm, which was made of lead (Pb). In order to acquire the attenuation data of the sample for attenuation correction simultaneously, an ideal energy-integrating detector with pixel size of 100 μm was placed 0.5 m downstream from the sample.

The sample was a cylinder of polymethyl methacrylate (PMMA) of diameter 2.5 cm, inside which there were five contrast agent containers of diameter 5.0 mm. The contrast agents were water solutions loaded with gadolinium (Gd), and the weight fractions of Gd were 0.2, 0.5, 1.0, 2.0 and 4.0 wt%, respectively. For element Gd, its K -edge is located at $E_K = 50.23$ keV and its K_{α} lines are located at 43.00 keV ($K_{\alpha 1}$) and 42.31 keV ($K_{\alpha 2}$) (Bearden, 1967). During the simulation, a 5 keV energy interval, ranging from 40 keV to 45 keV, of the photon-counting detector was set to collect the K_{α} fluorescent photons of Gd. The fluorescence yield $\omega_{K_{\alpha}}$ of Gd used in the simulation was 0.75046 (*i.e.* $\omega_{K_{\alpha 1}} = 0.48224$ and $\omega_{K_{\alpha 2}} = 0.26822$). For a CT scan, there were 360 projections acquired at a rotation step of 1° , in each of which the incident X-ray photon number used for simulation was 1.0×10^9 . These X-ray photons were uniformly distributed in a fan beam angle θ_c of 2.56 mrad confined by the collimator at the exit of the vacuum tube, corresponding to an FOV of ~ 3.0 cm at the sample.

2.3. Image reconstruction and attenuation correction

According to the imaging geometry in Fig. 2, the detection process of X-ray fluorescence photons can be divided into three steps:

(i) The incident X-rays with intensity I_0 and energy E_0 will be attenuated by the sample when they travel from point A to point P ; then the X-ray intensity $I(P)$ at P can be written as

$$I(P) = I_0 \exp\left[-\int_A^P \mu(E_0, \mathbf{r}) ds\right], \quad (3)$$

where μ is the linear attenuation coefficient of the sample and \mathbf{r} denotes a vector in Euclidean space.

(ii) The fluorescent X-ray photons are emitted isotropically if E_0 is higher than E_k ($E_0 = 60$ keV $>$ E_k in our simulation case), and the fluorescence intensity $I_{\text{XRF}}(P)$ at P is proportional to $I(P)$ and the local concentration $\rho_{\text{Gd}}(P)$ of Gd represented by mass percent,

$$I_{\text{XRF}}(P) = I(P) \mu_{\text{Gd,PE}}^m(E_0) \rho_{\text{Gd}}(P) \omega_{K_{\alpha}}, \quad (3b)$$

where $\mu_{\text{Gd,PE}}^m(E_0)$ is the photoelectric mass absorption coefficient of Gd at E_0 .

(iii) The fluorescent X-rays will be collected by the pinhole collimator C after propagating a distance d_p and then they are detected by the photon-counting detector D . Along this path, they are also attenuated by the sample from P to the boundary B . Hence, the fluorescence intensity $I_{\text{det}}(P, D)$ coming from P and detected at D can be expressed as

$$I_{\text{det}}(P, D) = I_{\text{XRF}}(P) \frac{\pi(\Phi/2)^2}{4\pi d_p^2} \exp\left[-\int_P^B \mu(E_{\text{XRF}}, \mathbf{r}) ds\right], \quad (3c)$$

where E_{XRF} is the spectrum-averaged energy of the K_{α} lines of Gd and its value is taken as 42.76 keV in the simulation.

Obviously the total fluorescence intensity detected at the i th bin D_i ($i = 1, 2, \dots, M$) of D is a volume integral of $I_{\text{det}}(P, D)$ over the pixel region $V_{P \rightarrow D_i}$ in the phantom inside a cone subtended by D_i toward the pinhole,

$$I_{\text{det},i} = \iiint_{V_{P \rightarrow D_i}} I_{\text{det}}(P, D) dV_P. \quad (4)$$

If the attenuation terms $\mu(E_0, \mathbf{r})$ and $\mu(E_{\text{XRF}}, \mathbf{r})$ in equations (3a) and (3c) are known, the relation between the detected fluorescence intensity \mathbf{I}_{det} of size $M \times 1$ and the unknown Gd concentration ρ_{Gd} of size $N \times 1$, after sample discretization, can be expressed in the form

$$\mathbf{I}_{\text{det}} = \mathbf{A} \rho_{\text{Gd}}, \quad (5)$$

where $\mathbf{A} = [a_{ij}]$ is the system matrix of size $M \times N$. Then, the ρ_{Gd} map can be reconstructed using an iterative algorithm called maximum-likelihood expectation maximization (MLEM) (Shepp & Vardi, 1982),

$$\rho_{\text{Gd},j}^{(k+1)} = \frac{\rho_{\text{Gd},j}^{(k)}}{\sum_{i=1}^M a_{ij}} \sum_{i=1}^M \frac{a_{ij} I_{\text{det},i}}{\sum_{j=1}^N a_{ij} \rho_{\text{Gd},j}^{(k)}} \quad (j = 1, 2, \dots, N). \quad (6)$$

Usually, the attenuation of the sample is unknown and non-negligible, hence an adjoint attenuation CT scan is necessary to calculate the system matrix \mathbf{A} and this can be realized easily since the energy of a Thomson scattering light source is continuously tunable. For determining the attenuation of the fluorescence photons, another attenuation CT scan was simulated at the same imaging geometry, while the photon energy was reduced to 42.76 keV with an r.m.s. bandwidth of 1% and only 180 projections were acquired at a sampling interval of 1° . Meanwhile, the incident X-ray photon number used at each projection was also 1.0×10^9 . The attenuation data of the phantom at both 60 keV and 42.76 keV were reconstructed using the well known ART-TV iterative algorithm and 180 projections were used in each attenuation reconstruction.

3. Results and discussions

To examine the efficiency of the scattering suppression scheme, two typical X-ray polarizations, *i.e.* horizontal polarization and vertical polarization, were used for comparison in the simulation. The comparison result between the two fluorescence spectra collected by the photon-counting detector with an ideal energy resolution (45 eV used here) is shown in Fig. 3. The spectrum was created by summing all of the pixels of the photon-counting detector after a full XFCT scan. Note that the K_{α} and K_{β} lines of Gd and the Compton and Thomson scattering backgrounds are all witnessed. The Compton scattering background mainly concentrates in the energy region of 48–59 keV, hence it can be effectively excluded by the photon-counting detector in the signal collection region of 40–45 keV in the simulation. Compared with the vertical polarization case, the Compton scattering background, in the horizontal polarization case, is suppressed by about 1.6 times, verified by calculating the mean value of typical L lines of Pb [*cf.* subfigure (2) of Fig. 3]. Hence, the scattering background in the fluorescence signal region is also reduced at the same level [*cf.* subfigure (1) of Fig. 3]. Different from the theoretical prediction described in Section 2.1, the improvement of scattering background is not substantial and this can be attributed to the deviation of scattering angles to the right one. In our simulation geometry, only Compton scattering occurring along the x -axis direction strictly satisfies the right angle described in Section 2.1, and the scattering from other parts of the phantom is still significant. By restricting the detected energy range of fluorescent signal and using the X-rays with horizontal linear polarization, the scattering background can be reduced to a negligible level, hence no scattering correction is needed before the CT reconstruction.

The sinogram (projection data, 360×400) of the sample is shown in Fig. 4. The contrast agents with different Gd concentrations can be discriminated. Meanwhile, the self-

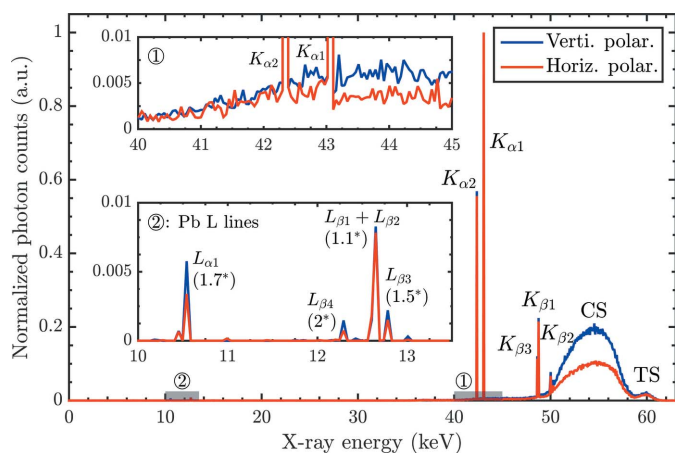


Figure 3 Comparison between two typical fluorescence spectra detected by the photon-counting detector. CS: Compton scattering; TS: Thomson scattering. *The ratio between the vertical polarization spectrum and the horizontal polarization spectrum at the corresponding L lines of Pb.

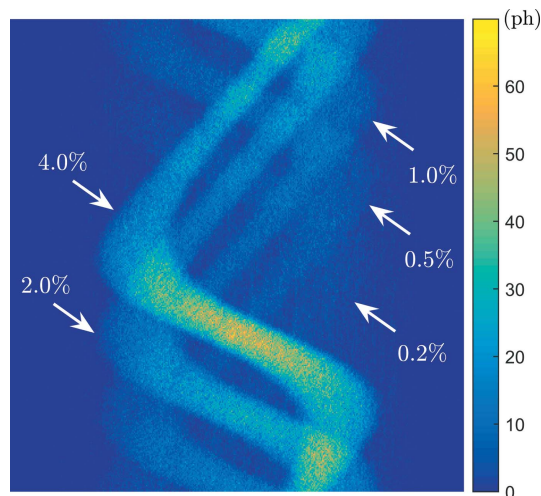


Figure 4 Sinogram of the phantom in the XFCT simulation.

absorption effect and the non-sinusoidal nature, due to the pinhole size influence, of the sinogram can also be witnessed. Based on this sinogram, the Gd concentration map can be reconstructed and the results are shown in Fig. 5. The reconstruction results with and without attenuation correction are all depicted in this figure, and they are all expressed in relative values. Also shown in Fig. 5 are the attenuation reconstruction results of the phantom at 60 keV and 42.76 keV, which are used to calculate the attenuation terms in system matrix \mathbf{A} . Note that the five contrast agents can be identified in the attenuation-corrected XFCT image [*cf.* Fig. 5(b)], while the contrast agent with Gd concentration of 0.2% can hardly be

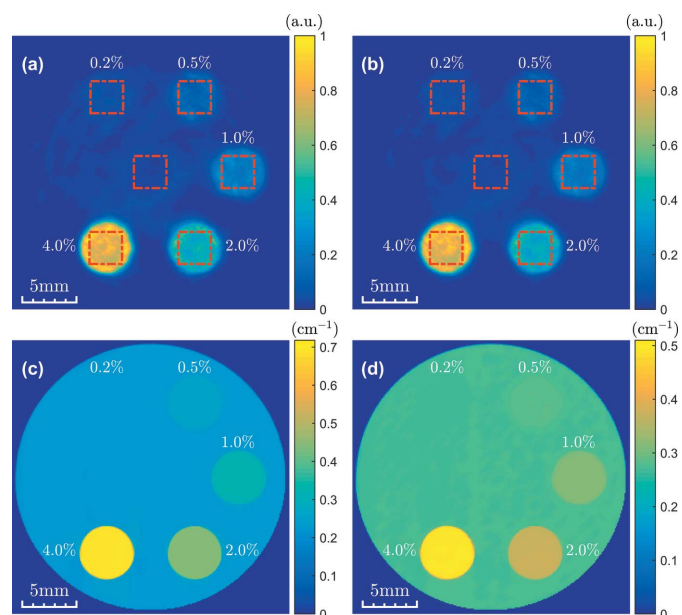


Figure 5 Gd concentration maps reconstructed (a) without and (b) with attenuation correction and the attenuation CT of the phantom reconstructed at (c) 60 keV and (d) 42.76 keV. The red dotted squares in the upper images are ROIs chosen for the quantitative analysis of the reconstructed results.

discriminated from the background in the attenuation CT results [cf. Figs. 5(c) and 5(d)]. In order to quantitatively analyze the reconstruction results, six regions of interest (ROIs) highlighted by red dotted squares in Figs. 5(a) and 5(b) are chosen. The relation between the reconstructed value S averaged over the ROI pixels in Fig. 5(b) and the actual Gd concentration ρ_{Gd} is plotted in Fig. 6. Also shown in Fig. 6 is the linear fitting result between S and ρ_{Gd} . Obviously, there is a good linear relation between the reconstructed result and the Gd concentration with $r^2 = 0.9999$. Using this relation for calibration, the relative values in the reconstructed images can be expressed by actual concentration values for quantitatively absolute measurement.

3.1. The influence of phantom attenuation

Compared with the reconstruction result in Fig. 5(a), the image contrast reconstructed with attenuation correction in Fig. 5(b) is improved significantly. To quantitatively analyze this contrast improvement, the contrast-to-noise ratio (CNR) is calculated. The CNR is defined as

$$\text{CNR} = \frac{S_{\text{Gd}} - S_{\text{BG}}}{\sigma_{\text{BG}}}, \quad (7)$$

where S_{Gd} and S_{BG} are the means of the ROI pixel values in the Gd and PMMA regions, respectively, and σ_{BG} is the standard deviation in the same ROI region of the PMMA. The calculated CNR results are depicted in Fig. 7 and also given in Table 1. Obviously the CNR of the reconstructed result with attenuation correction is higher than that of the corresponding result without attenuation correction. Based on the CNR results, we can also evaluate the contrast agent detectability. According to the Rose criterion, an object's CNR must exceed 3–5 in order to be detectable (Rose, 2013). To determine the actual value, we introduce another evaluation index called the limit of detection (LOD) with 95% confidence, which is defined as (Currie, 1968)

$$\text{LOD} = S_{\text{BG}} + 3.29\sigma_{\text{BG}}. \quad (8)$$

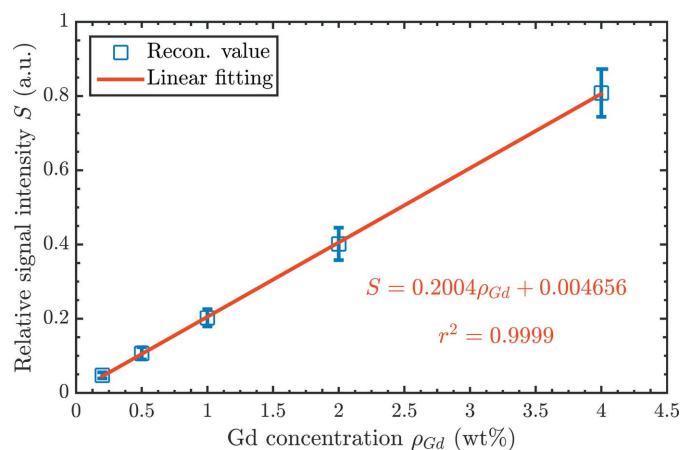


Figure 6 Relation between the reconstructed result and the actual Gd concentration. The reconstruction value is a mean over all pixels in the ROI and the error bar is the corresponding standard deviation.

Table 1 CNR comparison for different reconstruction modalities.

Gd concentration (wt%)	Original data	Attenuation correction	K-edge subtraction
0.2	3.71	3.98	1.96
0.5	11.50	13.94	13.35
1.0	23.67	29.99	32.60
2.0	47.95	63.38	71.56
4.0	92.75	131.58	152.68

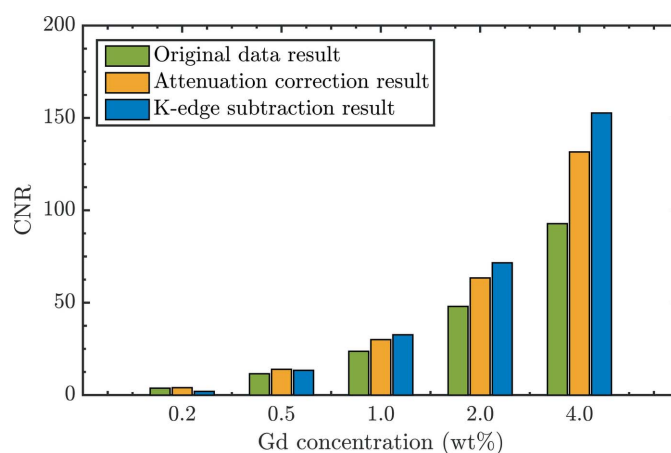


Figure 7 Comparison of the CNRs in XFCT reconstructed with and without attenuation correction and K-edge subtraction CT.

This gives a CNR threshold of 3.29 with 95% confidence. Based on this criterion, the four contrast agents with higher Gd concentration in XFCT can be clearly detected ($\text{CNR} > 5$, cf. Table 1) and the contrast agent with 0.2 wt% Gd concentration in XFCT can be identified with a confidence of more than 95% ($\text{CNR} > 3.29$, cf. Table 1). Since the attenuation correction can enhance the CNR in XFCT and a higher CNR means a lower LOD, it is necessary to correct the phantom attenuation to improve the LOD in XFCT.

3.2. The necessity of one full cycle sampling

For conventional attenuation CT in parallel or quasi-parallel (small fan angle) imaging geometry, 180° angular sampling is enough as its reconstruction and sampling at opposing angles cannot provide more information. However, in the XFCT using pinhole geometry the detected fluorescence signal changes with distance to the pinhole due to the self-absorption effect, hence sampling at opposing angles still provides additional information. For comparison, an XFCT of the phantom is reconstructed using 180° angular sampling at 1° intervals. In order to keep the same photon statistics as the case of 360° angular sampling, the incident X-ray photon number in each projection is doubled. The reconstruction result is shown in Fig. 8. It is obvious that the Gd maps are more noisy and the artefacts, especially around the discs of 2.0% and 4.0%, are stronger compared with the reconstructed result in Fig. 5(b). Therefore, one full cycle (360°) sampling

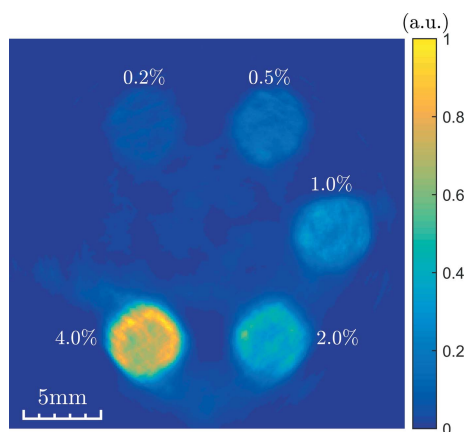


Figure 8
Attenuation-corrected XFCT of the phantom reconstructed using 180° angular sampling at 1° intervals.

becomes necessary when the attenuation of the phantom cannot be neglected.

3.3. The influence of sampling interval

The sampling interval is an important factor that can affect the reconstruction quality of XFCT and the imaging time. To demonstrate this influence, the phantom is reconstructed at different sampling intervals, and the results are shown in Fig. 9. Since the data acquisition of attenuation CT is more efficient than its counterpart XFCT, the attenuation CT of the phantom with high accuracy can be easily obtained. Hence, we only focus on the influence of XFCT reconstruction on the image quality without considering the errors introduced by attenuation CT reconstruction due to the sparse sampling, and the attenuation data in Figs. 5(c) and 5(d) are used for

attenuation correction here and below. From Fig. 9, it can be seen that the sampling interval plays an important role in the accurate XFCT reconstruction. When the sampling interval increases to 20°, the disc of 0.2% can hardly be distinguished from the background. Using a higher sampling interval [cf. Figs. 9(e) and 9(f)], the reconstruction results are seriously degraded by the artefacts caused by the angular under-sampling.

In order to quantitatively analyze the influence of the sampling interval on image reconstruction, the relative error R_e is calculated, and is defined as

$$R_e = \left[\frac{\sum_{j=1}^N (\rho_{Gd,j} - \rho_{Gd,j}^*)^2}{N} \right]^{1/2}, \quad (9)$$

where $\rho_{Gd,j}$ and $\rho_{Gd,j}^*$ are the reconstructed value of the j th pixel after calibration and its corresponding expected value, respectively, and N is the number of pixels in the reconstruction region. The calculated result is shown in Fig. 10. Notice that the relative error R_e is a monotonically increasing function of the sampling interval. When the sampling interval is less than 5°, R_e increases slowly and the influence of the sampling interval on the reconstruction quality is trivial [cf. Figs. 5(b) and 9(b)]. While the sampling interval exceeds 10°, R_e increases rapidly and the reconstruction quality of the phantom deteriorates seriously [cf. Fig. 9(c)–9(f)]. Therefore, the 5° sampling interval is a better choice in terms of the improvement of imaging time.

3.4. Comparison between XFCT and K -edge subtraction CT

Since the attenuation data of the phantom are reconstructed at energies both above and below the K -edge of Gd

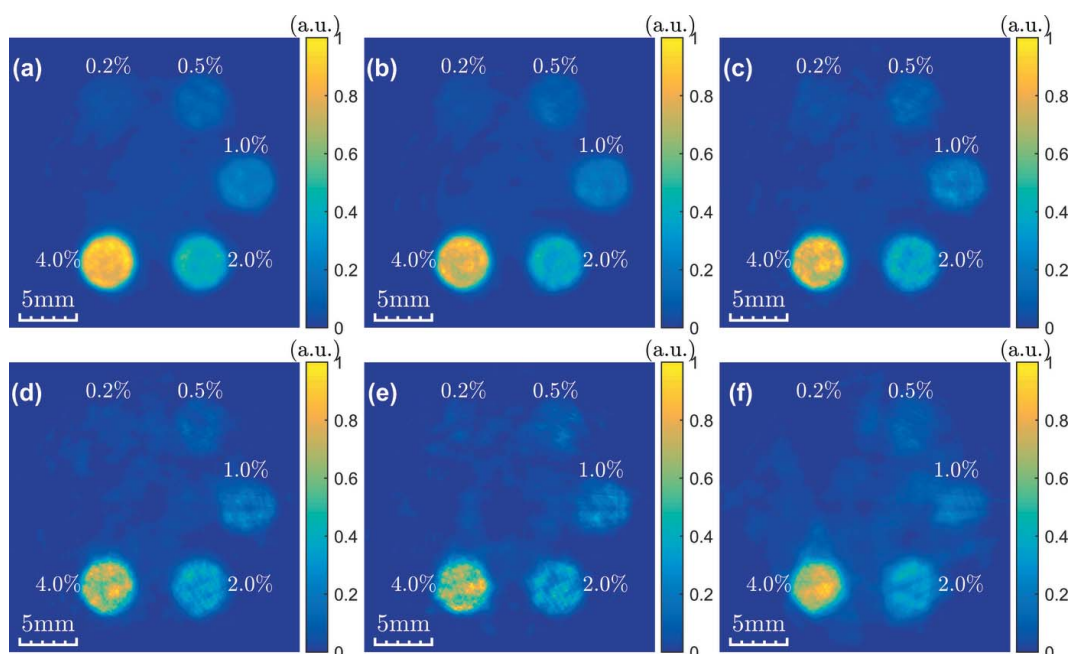


Figure 9
Attenuation-corrected XFCT of the phantom reconstructed at different sampling intervals over 360°: (a) 2°, (b) 5°, (c) 10°, (d) 20°, (e) 30° and (f) 40°.

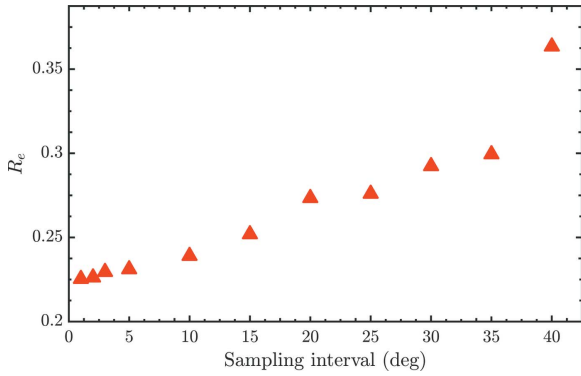


Figure 10
Relation between the relative error R_e and the sampling interval.

[*cf.* Figs. 5(c) and 5(d)], a K -edge subtraction can be easily realized, *i.e.*

$$\Delta\mu_K(\mathbf{r}) = \mu(E_{K^+}, \mathbf{r}) - \mu(E_{K^-}, \mathbf{r}), \quad (10)$$

where E_{K^+} and E_{K^-} are 60 keV and 42.76 keV in the simulation, respectively. The result is shown in Fig. 11. Obviously, the disc of 0.2% is still indiscernible from the background. This can also be confirmed by the Rose criterion ($\text{CNR} < 3$, *cf.* Table 1). For quantitative analysis of the result, six ROIs chosen in the quantitative analysis of the XFCT result are also taken into consideration. The CNR of the K -edge subtraction CT is calculated and depicted in Fig. 7. Compared with the XFCT result, the CNR values for 0.2 and 0.5 wt% Gd in the K -edge subtraction CT are reduced by 2.03 (*i.e.* 3.98/1.96, *cf.* Table 1, similarly hereinafter) and 1.04 times, respectively. Meanwhile, the CNR values for 1.0, 2.0 and 4.0 wt% Gd in the K -edge subtraction CT are improved by 1.09 (*i.e.* 32.60/29.99, *cf.* Table 1, similarly hereinafter), 1.13 and 1.16 times than their counterparts in XFCT, respectively. Since the total incident photon flux used for reconstruction is the same (360 projections for XFCT while 180 projections for each attenuation CT, and the same incident photon number in each projection), the CNR comparison between XFCT and K -edge

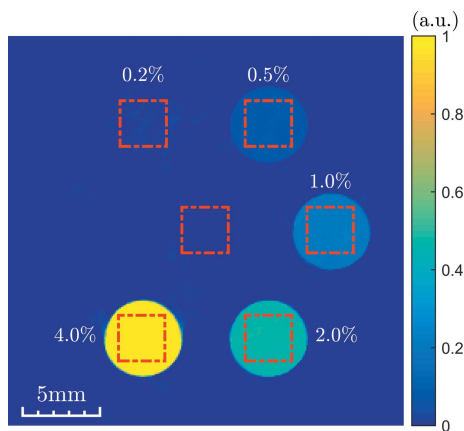


Figure 11
Normalized K -edge subtraction CT of the phantom. The red dotted squares in the image are the same ROIs as in Figs. 5(a) and 5(b), chosen for the quantitative analysis of the reconstructed results.

subtraction CT is fair. This result shows that XFCT has advantage over K -edge subtraction CT for contrast agents with lower concentration, and a similar conclusion was also drawn in previous works (Bazalova *et al.*, 2012; Feng *et al.*, 2014).

3.5. The influence of incident X-ray photon number

Usually, the fluorescence yield is low, hence the incident X-ray photon number used to excite the characteristic fluorescence emission plays an important role in the accurate XFCT reconstruction. To discuss this problem, simulations using different incident X-ray photon numbers are carried out with the sampling strategy unchanged (*i.e.* 360° sampling at 1° intervals). The reconstruction results are shown in Fig. 12. As expected, the reconstructed image quality becomes worse with the decrease of the incident X-ray photon number. To quantitatively analyze the influence, the LOD defined in Section 3.1 is evaluated and the result is shown in Fig. 13. Here, the LOD is expressed in units of wt% based on the calibrated conversion in Fig. 6. It is obvious that 5.0×10^8 incident X-ray photons per projection are needed in order to accurately retrieve the contrast agent with Gd concentration of 0.2%. When a higher Gd concentration of 1.0% is used, the incident X-ray photon number per projection can be reduced to 1.0×10^7 for its accurate reconstruction.

3.6. Estimation of imaging time

Based on the above discussion, 5.0×10^8 incident X-ray photons per projection are necessary to accurately reconstruct the phantom in our imaging geometry. For the sampling strategy using 360° at 1° intervals, the total incident X-ray photon number of a whole CT scan is 1.8×10^{11} . These photons are uniformly distributed in the fan of $\theta_c = 2.56$ mrad and 100 μm height at 12.5 m downstream of the IP, corresponding to a photon density of 5.6×10^{10} photons mm^{-2} . By extending this 2D model to 3D, the incident X-ray photon number in a cone of the same polar angle at the same distance can be easily calculated using the same photon density and the value is 4.5×10^{13} . The photons in this cone are just a small fraction of the total photon yield in a Thomson scattering light source and the fraction F can be calculated by integrating the probability density function $f(\theta, \phi)$ of the spatial distribution of scattered photons (Chi *et al.*, 2017b) over this cone,

$$F = \int_0^{2\pi} \int_0^{\theta_c/2} \frac{3}{8\pi} \frac{1}{\gamma^2(1 - \beta \cos \theta)^2} \times \left[1 - \frac{\sin^2 \theta \cos^2 \phi}{\gamma^2(1 - \beta \cos \theta)^2} \right] \sin \theta d\theta d\phi, \quad (11)$$

where $\gamma = 1/[(1 - \beta^2)^{1/2}]$ is the relativistic Lorentz factor and $\beta = v/c$ is the speed of electron normalized by the speed of light. For a commonly used head-on collision geometry between the electron bunch and laser pulse, γ can be calculated through the relation between the scattered X-ray peak energy E_x and the laser photon energy E_l ,

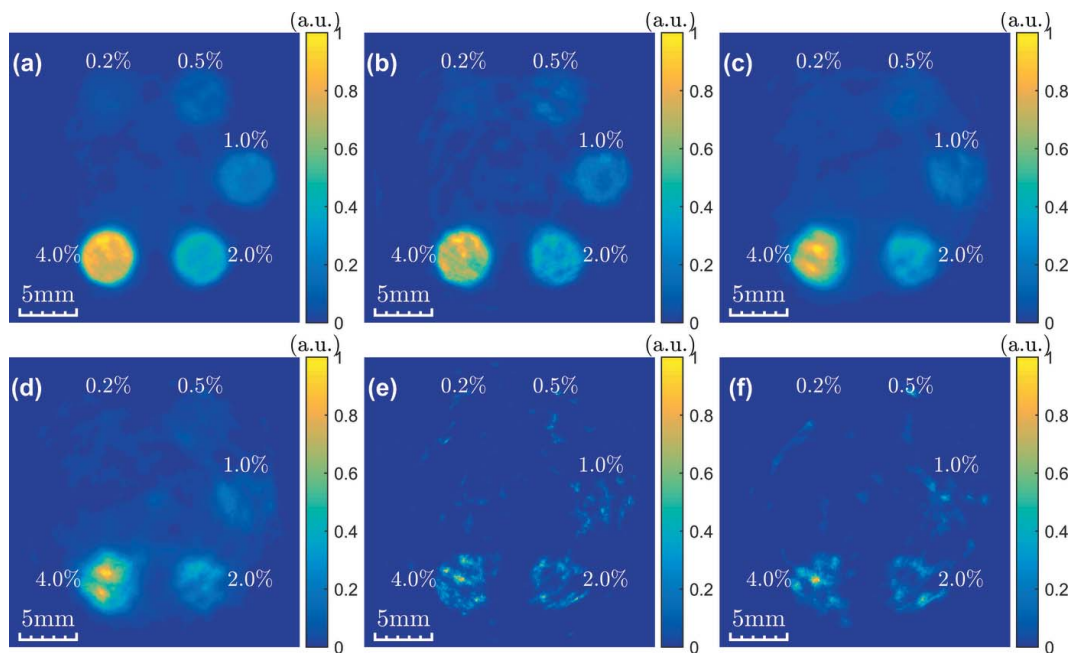


Figure 12 Attenuation-corrected XFCT of the phantom reconstructed using different incident X-ray photon numbers per projection: (a) 5.0×10^8 , (b) 1.0×10^8 , (c) 5.0×10^7 , (d) 1.0×10^7 , (e) 5.0×10^6 , and (f) 1.0×10^6 .

$$E_x = 4\gamma^2 E_1. \quad (12)$$

For an 800 nm laser commonly adopted in a Thomson scattering light source and 60 keV X-rays in our simulation, γ is 98.34 and F is 0.023. Hence, the total photon yield required for a whole XFCT scan is $4.5 \times 10^{13}/F = 2.0 \times 10^{15}$.

For a low-repetition Thomson scattering light source, e.g. the Tsinghua Thomson scattering X-ray source with photon yield of 2.0×10^8 photons s^{-1} (Chi *et al.*, 2018b), it would take ~ 116 days to finish the data acquisition for the whole CT with the same statistics. Even though a sampling interval of 5° can reduce the imaging time to ~ 23 days without significantly losing the reconstruction quality according to the results in Section 3.3, the huge amount of imaging time cannot be acceptable for practical XFCT applications. However, the photon flux of a Thomson scattering light source, based on the

high-repetition design technology, can reach 10^{13} photons s^{-1} and a series of laboratory-scaled facilities have been proposed and are under development at present (Jacquet, 2014; Deitrick *et al.*, 2018). Using these high-flux light sources, the data acquisition time of XFCT can be reduced to the minute or second level for the same parameters in our simulation, which is very attractive for *in vivo* imaging.

3.7. Analysis of the pulse pile-up effect

The pulse pile-up problem of a photon-counting detector can seriously affect the imaging quality when the photon flux is high. Here, we will analyze the potential pulse pile-up in our imaging geometry. The typical X-ray pulse length of a Thomson scattering light source is very short (ps–fs), far below the time resolution of a photon-counting detector. In order to avoid the pulse pile-up problem, the photon number of fluorescent X-rays detected per pixel on the detector cannot exceed 1 in one incident X-ray pulse. Hence, the photon yield Y per pulse should meet the following requirement,

$$\frac{Y F}{\pi [R_1 \tan(\theta_c/2)]^2} \mu_{Gd,PE}^m(E_0) \rho_{Gd}(P) \times V_{Gd} \omega_{K\alpha} \frac{\pi(\Phi/2)^2}{4\pi d_p^2} \frac{1}{N_{pix}} \leq 1, \quad (13)$$

where V_{Gd} is the phantom volume containing Gd inside the fan beam and $N_{pix} = 250$ [i.e. $(2.5 \text{ cm}/100 \mu\text{m})(d_2/d_1)$] is the number of effective detector pixels collecting fluorescent X-ray photons. For conservative estimate, we neglect the phantom attenuation in equation (13) and assume that the phantom is fully filled with contrast agent with Gd concentration of 4.0 wt%. Thus, the value of V_{Gd} is $\sim 49.1 \text{ mm}^3$. The

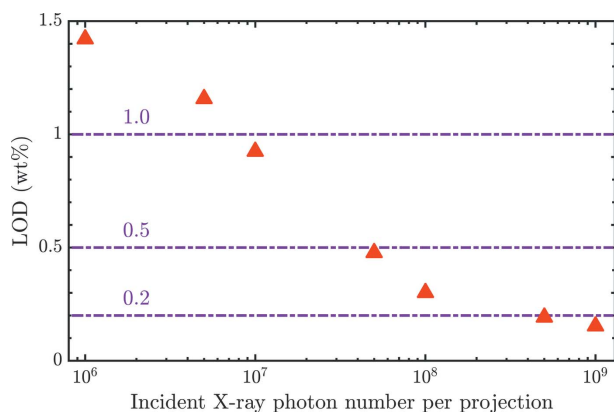


Figure 13 Relation between the LOD and the incident X-ray photon number used per projection.

photoelectric mass absorption coefficient $\mu_{\text{Gd,PE}}^m(E_0)$ of Gd at E_0 (60 keV) can be obtained from the software *XOP* (version 2.4) (see <http://www.esrf.eu/Instrumentation/software/data-analysis/xop2.4> for details) and its value is $11.3128 \text{ cm}^2 \text{ g}^{-1}$. The distance d_p can be taken as an approximate value, *i.e.* $d_p \simeq d_1 = 2.0 \text{ cm}$, and other parameters in equation (13) are the same as before. Substituting these parameters into equation (13), we can calculate the photon yield $Y \leq 1.2 \times 10^{11} \text{ photons pulse}^{-1}$. This value limits the highest photon yield per pulse of a Thomson scattering light source to avoid the pulse pile-up problem using our imaging geometry.

For a Thomson scattering light source with low repetition, the photon yield cannot reach the above limitation at present and the pulse pile-up cannot occur for fluorescent X-ray photons excited by adjacent incident X-ray pulses; the pulse pile-up problem, therefore, can be neglected in our imaging geometry. For a Thomson scattering light source with high repetition [usually in continuous wave (CW) mode], the pulse pile-up for fluorescent X-ray photons excited by adjacent incident X-ray pulses can occur, while this problem cannot occur in one incident X-ray pulse because of its relatively low photon yield per pulse. To estimate this effect, we take the photon flux of $10^{13} \text{ photons s}^{-1}$ as an example. In this case, the photon flux of fluorescent X-rays on the photon-counting detector, based on the above analysis, is $\sim 83 \text{ photons pixel}^{-1} \text{ s}^{-1}$ (*i.e.* $10^{13}/1.2 \times 10^{11}$). However, the count rate for a photon-counting detector can reach $0.01\text{--}10 \text{ Mcounts s}^{-1} \text{ pixel}^{-1}$ now (Taguchi & Iwaczyk, 2013) and it is far above the photon flux of fluorescent X-rays. Therefore, the pulse pile-up can also be neglected in our imaging geometry for a high-repetition Thomson scattering light source with photon flux of $10^{13} \text{ photons s}^{-1}$.

4. Conclusion and outlook

The excellent beam quality, small footprint and moderate cost of Thomson scattering X-ray sources provide a promising prospect for XFCT in laboratories and hospitals. In this paper, the feasibility of linearly polarized XFCT based on this type of light source has been studied by Monte Carlo simulations. The improvement of Compton scattering background has been verified by using X-rays with horizontal linear polarization. An accurate image of the Gd-containing phantom with Gd concentration ranging from 0.2 to 4.0 wt% has been reconstructed with improved CNR after attenuation correction. Compared with *K*-edge subtraction imaging, the CNR improvement of XFCT at low Gd concentrations of 0.2 and 0.5 wt% has been demonstrated. Using a high-flux Thomson scattering light source (*e.g.* $10^{13} \text{ photons s}^{-1}$), XFCT can be realized at the minute or second level without introducing any pulse pile-up problem, which is very promising for *in vivo* imaging. However, the scattering suppression is not significant in the current work due to the pinhole-collimated imaging geometry. This limitation can be resolved by using a parallel-hole collimation, such as an X-ray polycapillary. The high spatial resolution and large collection angle of an X-ray polycapillary will further improve the imaging time, and

relevant investigations on this topic will be carried out in the near future.

Funding information

Funding for this research was provided by: Fundamental Research Funds for the Central Universities (grant No. 310421105); National Natural Science Foundation of China (grant No. 11905011).

References

- Agostinelli, S., Allison, J., Amako, K., Apostolakis, J., Araujo, H., Arce, P., Asai, M., Axen, D., Banerjee, S., Barend, G., Behner, F., Bellagamba, L., Boudreau, J., Broglia, L., Brunengo, A., Burkhardt, H., Chauvie, S., Chuma, J., Chytráček, R., Cooperman, G., Cosmo, G., Degtyarenko, P., Dell'Acqua, A., Depaola, G., Dietrich, D., Enami, R., Feliciello, A., Ferguson, C., Fesefeldt, H., Folger, G., Foppiano, F., Forti, A., Garelli, S., Giani, S., Giannitrapani, R., Gibin, D., Gómez Cadenas, J. J., González, I., Gracia Abril, G., Greeniaus, G., Greiner, W., Grichine, V., Grossheim, A., Guatelli, S., Gumplinger, P., Hamatsu, R., Hashimoto, K., Hasui, H., Heikkinen, A., Howard, A., Ivanchenko, V., Johnson, A., Jones, F. W., Kallenbach, J., Kanaya, N., Kawabata, M., Kawabata, Y., Kawaguti, M., Kelner, S., Kent, P., Kimura, A., Kodama, T., Kokoulin, R., Kossov, M., Kurashige, H., Lamanna, E., Lampén, T., Lara, V., Lefebvre, V., Lei, F., Liendl, M., Lockman, W., Longo, F., Magni, S., Maire, M., Medernach, E., Minamimoto, K., Mora de Freitas, P., Morita, Y., Murakami, K., Nagamatu, M., Nartallo, R., Nieminen, P., Nishimura, T., Ohtsubo, K., Okamura, M., O'Neale, S., Oohata, Y., Paech, K., Perl, J., Pfeiffer, A., Pia, M. G., Ranjard, F., Rybin, A., Sadilov, S., Di Salvo, E., Santin, G., Sasaki, T., Savvas, N., Sawada, Y., Scherer, S., Sei, S., Sirotenko, V., Smith, D., Starkov, N., Stoecker, H., Sulkimo, J., Takahata, M., Tanaka, S., Tcherniaev, E., Safai Tehrani, E., Tropeano, M., Truscott, P., Uno, H., Urban, L., Urban, P., Verderi, M., Walkden, A., Wander, W., Weber, H., Wellisch, J. P., Wenaus, T., Williams, D. C., Wright, D., Yamada, T., Yoshida, H. & Zschiesche, D. (2003). *Nucl. Instrum. Methods Phys. Res. A*, **506**, 250–303.
- Bazalova, M., Kuang, Y., Prax, G. & Xing, L. (2012). *IEEE Trans. Med. Imaging*, **31**, 1620–1627.
- Bearden, J. A. (1967). *Rev. Mod. Phys.* **39**, 78–124.
- Chi, Z., Du, Y., Huang, W. & Tang, C. (2017a). *J. Appl. Phys.* **122**, 234903.
- Chi, Z., Du, Y., Huang, W. & Tang, C. (2018a). *J. Appl. Phys.* **124**, 124901.
- Chi, Z., Du, Y., Yan, L., Wang, D., Zhang, H., Huang, W. & Tang, C. (2018b). *J. Synchrotron Rad.* **25**, 1797–1802.
- Chi, Z., Yan, L., Du, Y., Zhang, Z., Huang, W., Chen, H. & Tang, C. (2017b). *Nucl. Instrum. Methods Phys. Res. B*, **402**, 364–369.
- Currie, L. A. (1968). *Anal. Chem.* **40**, 586–593.
- Deitrick, K., Krafft, G., Terzić, B. & Delayen, J. (2018). *Phys. Rev. Accel. Beams*, **21**, 080703.
- Feng, P., Cong, W., Wei, B. & Wang, G. (2014). *IEEE Trans. Biomed. Eng.* **61**, 975–985.
- Hartemann, F. V., Brown, W. J., Gibson, D. J., Anderson, S. G., Tremaine, A. M., Springer, P. T., Wootton, A. J., Hartouni, E. P. & Barty, C. P. J. (2005). *Phys. Rev. ST Accel. Beams*, **8**, 100702.
- Jacquet, M. (2014). *Nucl. Instrum. Methods Phys. Res. B*, **331**, 1–5.
- Petrillo, V., Bacci, A., Curatolo, C., Drebot, I., Giribono, A., Maroli, C., Rossi, A., Serafini, L., Tomassini, P., Vaccarezza, C. & Variola, A. (2015). *Phys. Rev. ST Accel. Beams*, **18**, 110701.
- Rose, A. (2013). *Vision: Human and Electronic*. Springer Science & Business Media.
- Shepp, L. A. & Vardi, Y. (1982). *IEEE Trans. Med. Imaging*, **1**, 113–122.
- Taguchi, K. & Iwaczyk, J. S. (2013). *Med. Phys.* **40**, 100901.